Materials and Design 197 (2021) 109207

Contents lists available at ScienceDirect

Materials and Design

journal homepage: www.elsevier.com/locate/matdes

Additively manufactured mesh-type titanium structures for cranial implants: E-PBF vs. L-PBF

Susanne Lewin [a,1,*], Ingmar Fleps [b,1], Jonas Åberg [a], Stephen J. Ferguson [b], Håkan Engqvist [a], Caroline Öhman-Mägi [a], Benedikt Helgason [b], Cecilia Persson [a]

[a] Div. of Applied Materials Science, Dept. of Materials Science and Engineering Sciences, Uppsala University, Uppsala, Sweden
[b] Institute for Biomechanics, ETH Zurich, Zurich, Switzerland

HIGHLIGHTS

- The study compares two additive manufacturing processes for mesh-type cranial implants, HIPed L-PBF and as-printed *E*-PBF.
- The HIPed L-PBF specimens showed superior mechanical strength in both the material (47%) and implant testing (87%).
- Geometrical deviations were obtained for the as-printed E-PBF implants (13–35%).
- The effect of geometrical deviations on implant performance was quantified, as enabled by mechanical simulations.

GRAPHICAL ABSTRACT

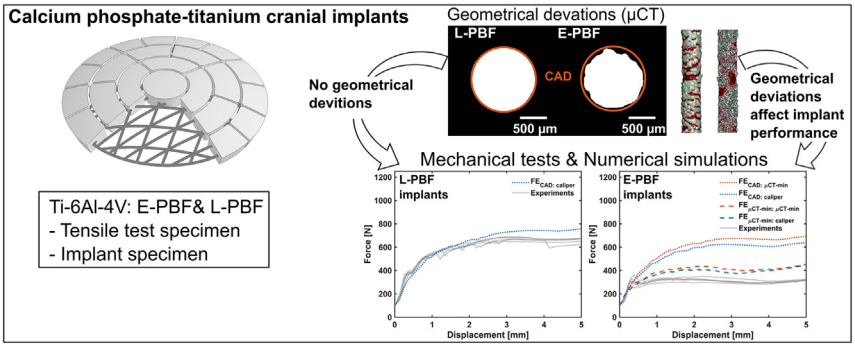

ARTICLE INFO

Article history:
Received 18 June 2020
Received in revised form 2 October 2020
Accepted 2 October 2020
Available online 6 October 2020

Keywords:
Additive manufacturing
Electron beam melting
Powder bed fusion
Finite element models
Surface roughness
Cranial implant

ABSTRACT

A patient-specific titanium-reinforced calcium phosphate (CaP–Ti) cranial implant has recently shown promising clinical results. Currently, its mesh-type titanium structure is additively manufactured using laser beam powder bed fusion (L-PBF). Nevertheless, an electron-beam (E-PBF) process could potentially be more time efficient. This study aimed to compare the geometrical accuracy and mechanical response of thin titanium structures manufactured by L-PBF (HIPed) and E-PBF (as-printed). Tensile test (ø = 1.2 mm) and implant specimens were manufactured. Measurements by µCT revealed a deviation in cross-sectional area as compared to the designed geometry: 13–35% for E-PBF and below 2% for L-PBF. A superior mechanical strength was obtained for the L-PBF specimens, both in the tensile test and the implant compression tests. The global peak load in the implant test was 457 ± 9 N and 846 ± 40 N for E-PBF and L-PBF, respectively. Numerical simulations demonstrated that geometrical deviation was the main factor in implant performance and enabled quantification of this effect: 34–39% reduction in initial peak force based on geometry, and only 11–16% reduction based on the material input. In summary, the study reveals an uncertainty in accuracy when structures of sizes relevant to mesh-type cranial implants are printed by the E-PBF method.

© 2020 The Authors. Published by Elsevier Ltd. This is an open access article under the CC BY license (http://creativecommons.org/licenses/by/4.0/).

1. Introduction

Advances in additive manufacturing (AM), clinical imaging, and computer aided design and manufacturing (CAD/CAM) have resulted in major improvements of several biomedical applications [1]. In cranial

* Corresponding author at: Div. of Applied Materials Science, Dept. of Materials Science and Engineering Sciences, Uppsala University, Box 35, 751 03 Uppsala, Sweden.
E-mail address: susanne.lewin@angstrom.uu.se (S. Lewin).
[1] These authors contributed equally to the study.

https://doi.org/10.1016/j.matdes.2020.109207
0264-1275/© 2020 The Authors. Published by Elsevier Ltd. This is an open access article under the CC BY license (http://creativecommons.org/licenses/by/4.0/).

reconstructions, the technological advances enable the production and successful implementation of patient-specific implant systems [1–4]. While these technologies have been adopted for clinical use, several material and design-related questions in the AM process remain to be investigated.

Patient-specific titanium cranial implants are commonly designed as mesh structures. The benefits of this approach are for example lighter structures, less material being implanted, and a reduction of metal artefacts in X-ray imaging [5]. However, thin structures with complex geometries add difficulties to AM since intricate support structures and additional post-processing might be required [6,7]. The accuracy and achievable feature size depend on the AM process (method, process parameters, layer thickness etc.) and on the material characteristics (powder particle size, composition etc.). For titanium alloys, the most commonly applied methods are two powder-bed fusion (PBF) processes in which metal powder is selectively melted using either an electron (E-PBF) or a laser beam (L-PBF) [8]. In general, smaller powder particles and decreased layer thicknesses are used in L-PBF, compared to E-PBF, due to current differences in beam spot size [9]. For this reason, the precision and resolution of the L-PBF technology is higher than the *E*-PBF technology [10–12]. The printed E-PBF parts also have a higher surface roughness than parts produced by L-PBF [11–13]. The rough surface will remain since post-processing is difficult to achieve in complex mesh structures. A rough surface topology has been found to be biologically beneficial for blood coagulation in vitro [14] and osseointegration in vivo [15]. However, the rough surface will affect the mechanical properties since surface defects can act as stress raisers and decrease the mechanical strength in comparison to the designed geometry [10–12]. As the size of a part is decreased, this effect will become more prominent due to the changed surface to volume ratio [13,16]. However, the E-PBF technology could be desirable for patient specific implants since the time from order to implant delivery is directly related to the waiting time for the patient [1]. In comparison to L-PBF, several factors could potentially allow for a shorter production time when using the E-PBF technology; a higher total deposition rate, less need for support structures, it allows stacking of parts and there is less need for thermal stress relief treatments [9,11–13]. An increased productivity by stacking of parts should be of importance also for patient-specific implants: although most patients usually need only one implant, patients requiring additional implants are not uncommon [3]. Furthermore, more than one patient frequently requires implants at the same time.

This study focuses on a new patient-specific titanium–reinforced calcium phosphate (CaP–Ti) cranial implant. The implant has shown promising clinical results [3,17,18], where the calcium phosphate (CaP) material has shown osteoconduction and osseointegration [3,18]. However, as CaP materials are inherently brittle, a titanium structure is incorporated to add structural support to the implant. As the current design involves small geometrical features, the smallest being 300 μm, the titanium structure is produced using L-PBF. The structures are also HIPed, which decreases the porosity and increases the ductility of the material. In a previous study, the mechanical properties of the implant were investigated [19]. Moreover, that study developed and evaluated a new implant design, which aimed to facilitate the AM production – with the purpose of reducing production time and cost [19]. The modifications in the design would potentially allow for the use of AM methods with a lower resolution. Consequently, this modified CaP–Ti implant would constitute an interesting case study for evaluating E-PBF for thin structures in biomedical applications. However, it would be important that the cranial implant still has sufficient strength. Cranial implant strength is commonly evaluated in comparison with clinically available implants, since no standardized mechanical requirements exists. Therefore, the mechanical strength of the CaP–Ti E-PBF produced implants should be evaluated in comparison with CaP–Ti L-PBF produced implants.

Numerical approaches in evaluation of design changes would be beneficial since they can save time and design costs. Finite element (FE) models of the CaP–Ti implant were recently validated against experimental data at two different loading rates, which make analysis of new design concepts possible [20]. However, before the E-PBF implant can be analyzed accurately by FE-models, the material property inputs, surface characteristics and accuracy of the manufacturing process must be evaluated and compared with L-PBF.

This study compares the mechanical characteristics of HIPed L-PBF and as-printed E-PBF Ti-6Al-4V tensile test specimens and CaP–Ti cranial implant specimens. To this end, tensile specimens for both manufacturing methods and corresponding cranial implants were mechanically tested. FE-models were used for quantifying the contribution of geometry and material inputs to the mechanical response of the implants.

2. Materials & methods

2.1. Tensile test specimen and implant specimen

Specimens for the tensile test were produced to correspond to the geometry of the titanium structure in the implants: the full gauge length was 10 mm and the diameter (ø) within the gauge length was 1.2 mm (Fig. 1a). The geometry was designed in a commercial CAD software (Rhinoceros 3D, release 5, Robert McNeel & Assoc., USA). The specimens were manufactured with material deposited in the longitudinal direction with an E-PBF (number of specimens; $n = 5$) or a L-PBF ($n = 5$) process in Ti-6Al-4V. Hot isostatic pressing (HIP) was only applied to the L-PBF samples, while both types of specimens were bead blasted. HIP was applied to resemble the process for the L-PBF printed Ti-6Al-4V structures in the clinically used CaP–Ti implants. All specimens were provided by OssDsign (OssDsign, Uppsala, Sweden).

The implant specimens (Fig. 1b) represent a generic shape with an idealized curved circular geometry (ø = 80 mm). The radius of the curvature was 90 mm, which corresponds to an average skull curvature [21,22]. The rods in the titanium mesh structure had a circular cross-section, with a diameter of 1.2 mm. The titanium structures were produced in medical grade 23 Ti-6Al-4V ELI by an E-PBF process, which was followed by bead blasting. During the manufacturing, the outer circumference of the titanium structure was oriented towards the building plate. The CaP formulation consisted of monetite (~86%), beta-tricalcium-phosphate (β-TCP; ~7%) and β-calcium pyrophosphate (β-CPP; ~7%), with a final porosity of approximately 40% [17]. All implant specimens ($n = 6$) were prepared by OssDsign (OssDsign, Uppsala, Sweden).

2.2. Geometrical deviations

Micro-computed tomography (μCT; SkyScan1176, Bruker Corp., Belgium) scans were acquired of the gauge length for one tensile test specimen manufactured by L-PBF and E-PBF. The specimens were scanned at 80 kV and 313 μA, with a Cu-Al filter at an isotropic voxel size of 8.67 μm. Cross-sectional images were reconstructed using NRecon (NRecon 1.7.1.0, Bruker Corp., Belgium) with the specimens aligned along the longitudinal axis. The reconstructed cross-sections (transversal plane) were segmented by an automatic global threshold [23]. Subsequently, the cross-sectional areas were obtained. The image processing was conducted in CTAn (CTAn 1.16.4.1, Bruker Corp., Belgium). The minimum (A_{min}), average (A_{mean}) and maximum (A_{max}) cross-sectional areas from the μCT analysis were compared to the cross-sectional area of the CAD geometry (A_{CAD}). Finally, 3D-models of the segmented volumes were exported as STL-files to be used as input geometry for the finite element models.

Further characterization of the surfaces of these specimens was conducted by scanning electron microscopy (SEM; Leo 1530, Zeiss, Germany) operating at 10 kV with a secondary electron detector. For the same tensile test specimen, the surface roughness was also investigated by optical profilometry (ZYGO NexView, Zygo Corporation, USA). The average roughness (S_a) and the peak-to-valley height (S_z) were

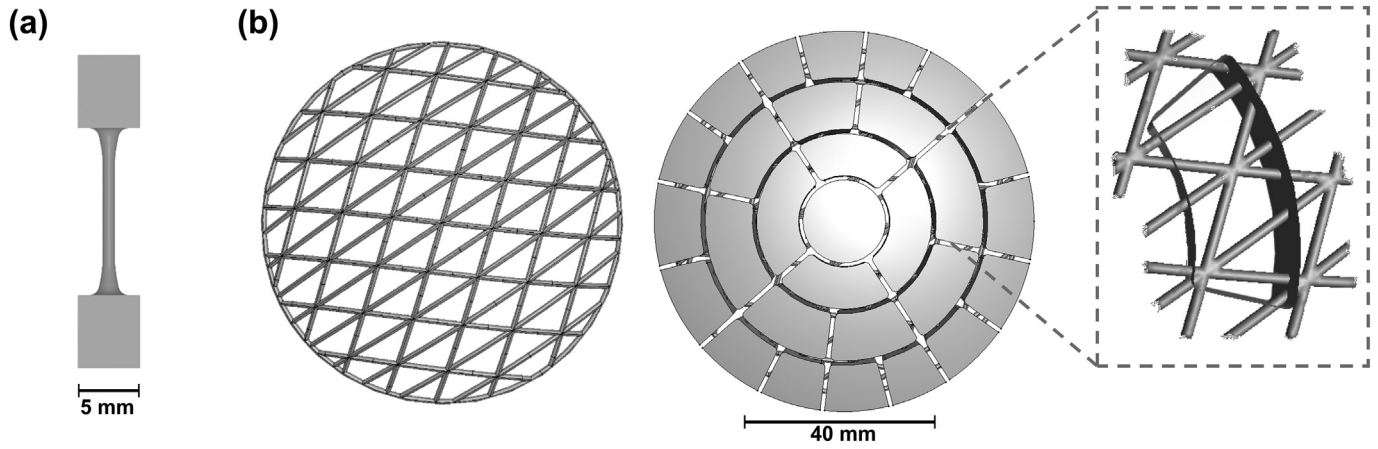

Fig. 1. Overview of the CAD geometry for the tensile (a) and implant specimen (b). The cross-sectional diameter of the titanium rods in both specimen types was 1.2 mm. The titanium structure in the implant is shown from the top (b). The full implant (ø = 80 mm) is shown together with the placement of one calcium phosphate tile over the titanium structure.

measured over an 850 × 850 μm surface. For each specimen type, three measurements were performed on the rectangular grip sections.

In addition, μCT analysis was conducted on two specimens (~5 mm in length) isolated from the titanium structures of the tested implants in this study (produced by E-PBF), but also on two specimens from implants tested in our previous study (produced by L-PBF). The scan settings and analysis procedure were the same as for the tensile specimens.

2.3. Tensile tests and hardness measurements

The tensile tests were performed according to ISO 6892. An exception from this test standard was the specimen dimensions, which were adapted to represent the titanium structure in the implants. The specimens were marked at the gauge length and the diameter of the specimens was measured by a caliper. The tensile tests ($n = 5$ for each group) were performed at a displacement rate of 1 mm/min in a universal test machine (AGS-X, Shimadzu Corporation, Japan). The tests were recorded by a high-speed camera (IDT Y8-S2, Integrated Design Tools, Inc., USA) at 100 FPS and a resolution of 1600 × 1200 pixels. To measure displacement, the distance between the markers was tracked during the test (GOM correlate V8, GOM GmbH, Germany).

Stress was calculated as the force measured by the load cell divided by the cross-sectional area of the specimens derived from caliper measurements ($A_{Caliper}$). Strain was calculated as the elongation of the specimen over the gauge length divided by the gauge length. Young's modulus (E), strain at break (ϵ_{UTS}), yield stress (σ_Y), and ultimate stress (σ_{UTS}) were calculated from the engineering stress-strain response for each specimen.

In order to characterize the mechanical properties without an effect of the surface roughness, Vickers hardness testing (MXT 50, Matsuzawa Co., Ltd., Japan) was performed on polished cross-sections. For one tensile test specimen of each type, seven indents were made with a 300 g load.

2.4. Tensile test simulations

Finite element (FE) models for the tensile specimens were created from both the CAD geometry (FE_{CAD}) and the STL-files from the μCT ($FE_{\mu CT\text{-}STL}$) for both L-PBF and E-PBF. All models were discretized in a commercial preprocessor (Ansa 17.1.0, Beta CAE Systems, Switzerland), the mesh had an element size of 50 μm.

The displacement of all nodes on the bottom of the models was constrained in the direction of load application. Step-wise displacement was applied to all the nodes on the top in order to resemble the experimental tensile test. The tensile specimens were modelled with first order tetrahedral elements (Ls-Dyna, element formulation 13). Material properties from the tensile tests (hereinafter referred to as *material inputs*) were used to define an elasto-plastic material model in the FE simulations (LS-Dyna, MAT 24). The Poisson's ratio was set to 0.3. The FE-models were solved with double precision in a commercial implicit solver (LS-Dyna R11.0.0, Livermore, CA, USA). The stresses were recalculated from the nominal stress and strain to the Cauchy stress and logarithmic strain before implementation into the models. Since deviations in the geometries were detected by the μCT analysis as compared to the caliper measurements, the cross-sectional areas obtained from the μCT analysis, i.e. A_{min} or A_{mean}, were used to recalculate the stress values and material inputs from the tensile test (obtained with $A_{caliper}$). The material inputs were used in the different models. The models were denoted by the type of geometry and the type of material inputs used ($FE_{\text{geometry: material input}}$): $FE_{\text{CAD: caliper}}$, $FE_{\mu\text{CT-STL: caliper}}$, $FE_{\mu\text{CT-STL: }\mu\text{CT-min}}$, $FE_{\text{caliper: caliper}}$, etc.

The force–displacement response from the simulations was compared to the experimental results. The reaction force in a cross-section in the middle of each model was evaluated in order to mimic the experimentally measured force. The displacement in each model was evaluated for the mean gauge length from which the displacement was measured in the experiment.

2.5. Mechanical testing of implant specimens

Details on the test-setup for the mechanical tests of the implants have been thoroughly described elsewhere [19]. In brief, a rigid hollow steel cylinder, was used to support the implants around the circumference. The conical contact surfaces of the steel cylinder had the same incline as the implant edges. This conical hollow steel cylinder is hereinafter referred to as the conical steel support. The setup was mounted in a universal testing machine (AGS-X, Shimadzu Corp., Japan). Next, a silicone rubber sheet (thickness of 5 mm) was placed on top of the implant as a soft tissue surrogate and a compressive load applied using a hemispherical indenter (ø = 40 mm). Five compression cycles were performed at 1 mm/min up to 100 N (for preconditioning). Subsequently, the implants were loaded until failure at the same loading rate. All manufactured E-PBF implant specimens ($n = 6$) were tested. The full test setup can be seen in Fig. 2a.

The displacement data was corrected for machine compliance and zeroed at a load of 3 N. The combined stiffness of the implant and silicone was calculated between 1.5 mm and 3 mm displacement, hereafter referred to as *construct stiffness*. The point at which the first CaP fracture occurred, defined by the first point of decrease in force, was noted in the force–displacement curves.

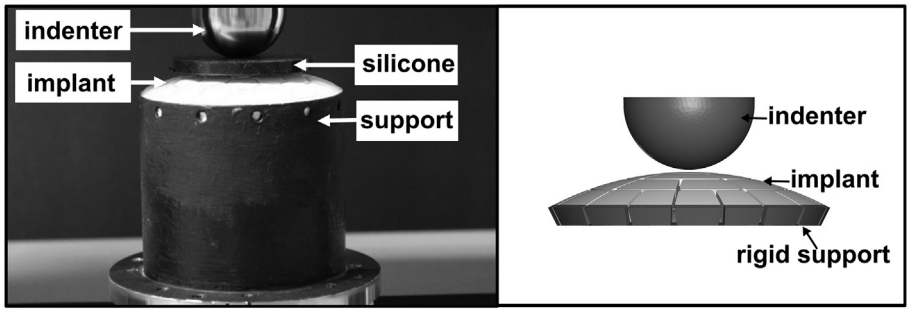

Fig. 2. The experimental test setup (reprinted with modification from [19]), and the corresponding FE-model.

2.6. Implant test simulations

For implants with titanium structures printed by L-PBF, the construction and validation of FE-models have been thoroughly described elsewhere [20]. A brief overview is provided below for clarity and context, together with changes made for investigating the E-PBF printed titanium. CAD-files of the titanium structure and the ceramic tiles, were obtained from the implant manufacturer (OssDsign, Uppsala, Sweden) (Fig. 1b) and models were created (FE_{CAD}). In addition, models were created where the diameter of the titanium structure was decreased to the minimum diameter obtained from the μCT measurements of the E-PBF implants. The corresponding model was denoted $FE_{\mu CT\text{-}min}$. The hemispherical indenter (ø = 40 mm), and the surface of the conical steel support below the specimen were modelled to match the experimental setup. All parts were semi-automatically discretized with tetrahedral elements in a commercial pre-processor (Ansa 17.1.0, Beta CAE Systems, Switzerland). The indenter and the conical steel support surface were modelled as a linear elastic material, with properties corresponding to steel ($E = 210$ GPa, and $\nu = 0.3$). All nodes on the outer edge of the support surface were fixed. The indenter was constrained from horizontal translation. Loading was applied by a uniform displacement on top of the indenter. Contact pairs were defined with a friction coefficient ($\mu = 0.3$), between the CaP tiles and the conical steel support surface, and between the indenter and the CaP tiles. The nodes of the CaP tiles were tied to the titanium. The FE-model including the implant, the indenter and the conical steel support surface (Fig. 2) consisted of 2,612,654 elements for the implant FE_{CAD}. The indenter and support surface were modelled with first order tetrahedral elements (LS-Dyna, element formulation 10). Tetrahedral elements of the first order were also used for the titanium structure and the ceramic tiles in the implant, but another element formulation that takes nodal pressure into account in order to reduce volumetric locking (LS-Dyna, element formulation 13) was used [25]. The FE-models were solved with double precision in a commercial implicit solver (LS-Dyna R11.0.0, Livermore, CA, USA).

An elasto-plastic material model was used for the titanium alloy (LS-Dyna, MAT 24). Material inputs were obtained from the previously described tensile tests, either calculated with the caliper measurements or the μCT measurements. The implant models were denoted by the type of geometry and material input. Models with CAD geometry were simulated with both E-PBF and L-PBF caliper based material inputs ($FE_{CAD:\ caliper}$). The reduced geometry, based on the minimum diameter from the E-PBF μCT measurements, were also simulated with both E-PBF and L-PBF caliper based material inputs ($FE_{\mu CT\text{-}min:\ caliper}$). Stresses were again recalculated from the nominal stress and strain to the Cauchy stress and logarithmic strain before implementation into the models. A material model with tension-compression asymmetry (LS-Dyna, MAT 124) was used for the CaP material. The CaP compressive material constants were based on previous testing preformed on the same CaP formulation [26]: $E = 7$ GPa, $\sigma_{UTS} = 13$ MPa and $\nu = 0.2$. In tension, σ_{UTS} was estimated to 1.6 MPa based on experiments on a similar CaP material [27]. Perfect plasticity was assumed both in tension and compression after the strain of failure was reached.

The response of each FE-model was compared to the corresponding experimental data. For this comparison, the compliance of the rubber sheet was subtracted from the experimental results. For the subtraction, a spline interpolation of silicone rubber test data was used (5 mm silicon sheet tested in compression at 1 mm/min with the same indenter as used in the implant testing). The response was plotted from a force of 100 N, where the displacement was set to zero. This was done to minimize the influence of the toe-region created by the rubber sheet. The force measured in the quasi-static tests was compared to the reaction force of the indenter, the initial peak load was compared before 4 mm displacement. Differences in the mechanical response due to differences in material inputs and differences in geometry were quantified through the initial peak load before 4 mm displacement.

2.7. Statistics

Statistical analysis was performed in R (version 3.5.2) [28]. The analyses were conducted to assess differences between as-printed E-PBF and HIPed L-PBF in the tensile test and the test of the implants. The groups were compared by a Welch two sample *t*-test, in which significant results were noted for a probability value $p < 0.05$.

3. Results

3.1. Geometrical deviations

The results from the μCT-based quantifications of the cross-sectional area can be seen in Fig. 3 and Table 1. For the E-PBF tensile specimen, the μCT and caliper measurements demonstrated a negative deviation in cross-sectional area compared to A_{CAD} of 18% (range: 13–25%). The E-PBF implant specimens had larger deviations ranging from 26% to 35%. For all HIPed L-PBF implant and tensile specimens, the μCT measurements demonstrated deviations below 2% (range: −2 to 0.9%).

The tensile specimens are visualized in Figs. 3 and 4. The magnitude of geometrical deviation for all specimens is presented in Fig. 3a. In Fig. 3b and c, cross-sections of each specimen are shown together with the cross-section from the CAD-geometry. The distributions of the cross-sectional areas are presented in histograms in Fig. 3d and e.

Table 1
Comparison of μCT measurements of the tensile ($n = 1$) and implant specimen ($n = 2$). The deviation in $A_{caliper}$, A_{min}, A_{mean} and A_{max} are compared to A_{CAD}. N/A = not applicable. E-PBF specimens were evaluated as-printed, and L-PBF specimens after HIP treatment.

	A_{CAD} vs. $A_{caliper}$ [%]	A_{CAD} vs. A_{min} [%]	A_{CAD} vs. A_{mean} [%]	A_{CAD} vs. A_{max} [%]
E-PBF: Tensile	−13.4	−25.4	−18.1	−12.9
E-PBF: Implant	N/A	−34.7	−30.4	−26.4
E-PBF: Implant	N/A	−32.1	−29.0	−25.7
L-PBF: Tensile	−0.8	−1.3	−0.7	0.3
L-PBF: Implant	N/A	−1.4	−0.5	0.9
L-PBF: Implant	N/A	−2.0	−0.9	0.3

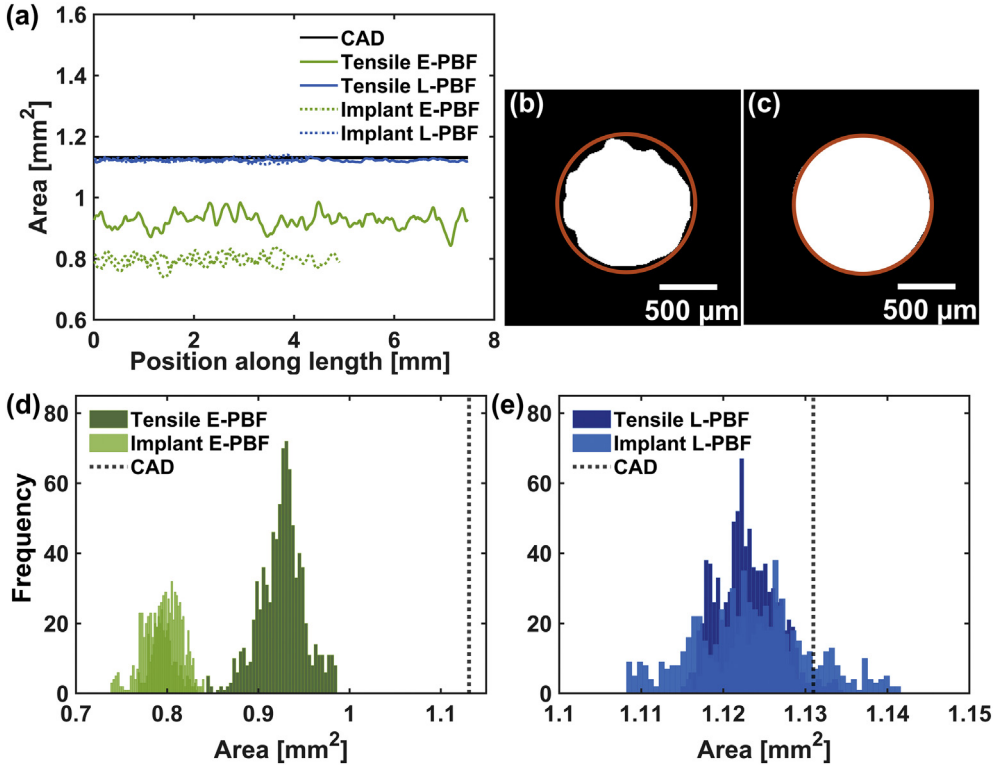

Fig. 3. Geometrical deviations in cross-sectional area for the tensile and implant specimens. The cross-sectional area along the specimen length, for the tensile specimens (solid lines), and specimens cut from the titanium structures of the implants (dotted lines) (a). In the graph, the as-printed E-PBF (green) and the HIPed L-PBF (blue) cross-sectional areas are compared to the designed CAD-geometry (black). Two cross-sections of tensile specimens produced by E-PBF (b) and L-PBF (c) are shown, where the red circle marks the corresponding CAD-geometry. In the histograms (number of bins = 40) the distribution of the cross-sectional area along the specimen length are shown for the E-PBF (d) and L-PBF (e) specimen. Both the tensile specimen ($n = 1$) and the implant specimens ($n = 2$) are included. The dotted black lines in the histograms show the designed area from the CAD-geometry. (For interpretation of the references to colour in this figure legend, the reader is referred to the web version of this article.)

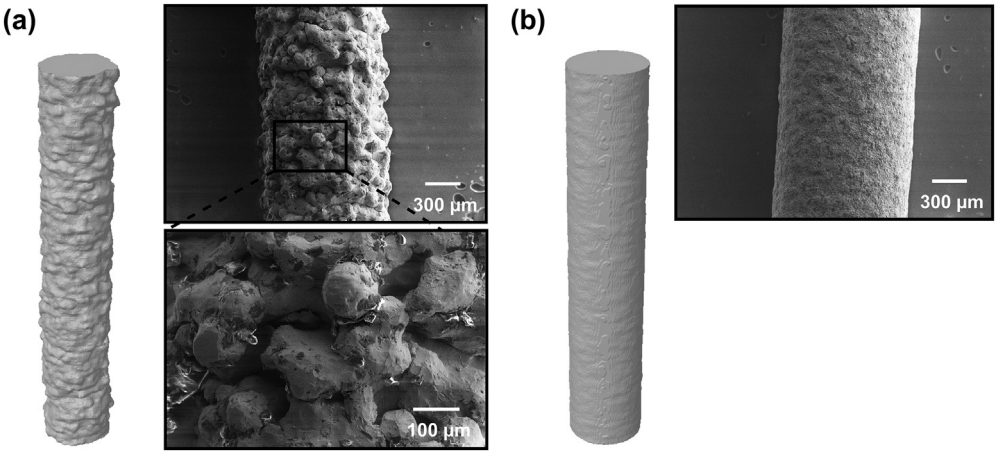

Fig. 4. µCT and SEM visualization of one tensile specimen from each group. 3D-volumes from the µCT and SEM surface characterizations for as-printed E-PBF (a) and HIPed L-PBF (b) specimens. The overview SEM images are at 100× magnification, and the enlargement (a) at 400× magnification.

The rough surface of the E-PBF specimen can be observed in Fig. 4a. Details of the surfaces can be observed in the SEM images, where partly melted particles are adhering to the surface in the E-PBF specimen. In contrast, the HIPed L-PBF specimen (4b) showed a much smoother surface, as expected.

The optical profilometry measurements resulted in an average S_a of 35.9 ± 1.9 µm for the E-PBF and 3.5 ± 0.2 µm for the L-PBF specimen. The average S_z was 211.0 ± 7.2 µm for the E-PBF and 34.4 ± 4.6 µm for the L-PBF specimen.

3.2. Tensile tests and hardness measurements

The material properties obtained from the tensile test, calculated from $A_{caliper}$, are presented in Table 2. The difference between E-PBF and L-PBF was significant ($p < 0.01$) for all material properties. As the stresses were calculated by normalizing with the µCT areas, the material properties changed accordingly (Fig. 5a-c). The A_{min} material properties, later used in the simulations, are presented in Table 2 for both the E-PBF and L-PBF specimens.

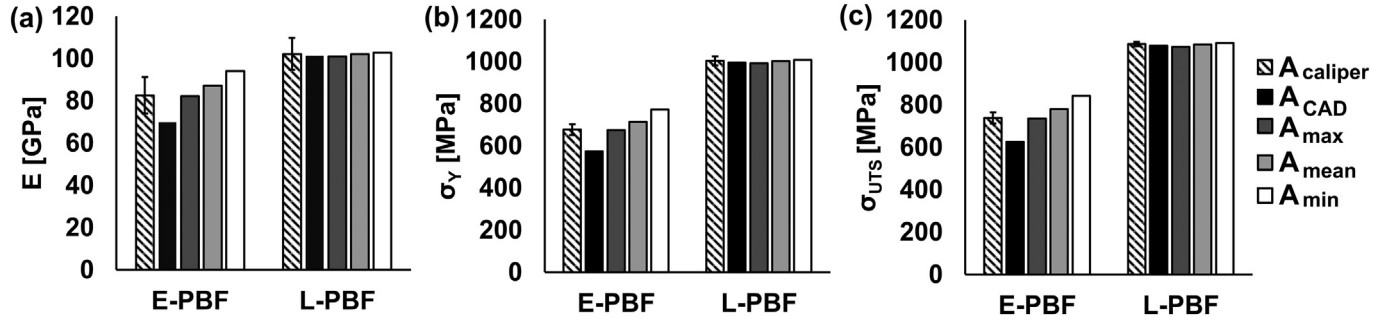

Fig. 5. The material properties E (a), σ_Y (b), and σ_{UTS} (c). The stresses have been calculated by: $A_{caliper}$, A_{CAD}, A_{max}, A_{mean}, and A_{min}. The results are shown for both the as-printed E-PBF and the HIPed L-PBF specimens.

Table 2
Material properties form the tensile tests. The area used in the calculation was $A_{caliper}$ (average ± standard deviation) or recalculated by A_{min}.

	E [GPa]	σ_Y [MPa]	σ_{UTS} [MPa]	elongation at break [%]
E-PBF: $A_{caliper}$	82.6 ± 8.6	677.4 ± 26.0	738.3 ± 26.0	3.1 ± 0.4
E-PBF: A_{min}	94.1	772.1	841.5	–
L-PBF: $A_{caliper}$	102.2 ± 7.5	1003.6 ± 21.1	1086.1 ± 10.1	10.7 ± 1.3
L-PBF: A_{min}	102.8	1009.0	1092.0	–

The average microhardness was 356 ± 6 $HV_{0.3}$ and 392 ± 4 $HV_{0.3}$ for the E-PBF and L-PBF specimen, respectively.

3.3. Tensile test simulations

For FE-models of the E-PBF tensile specimen, the force–displacement responses are presented in Fig. 6a. The force was underestimated when caliper-based material input was used in

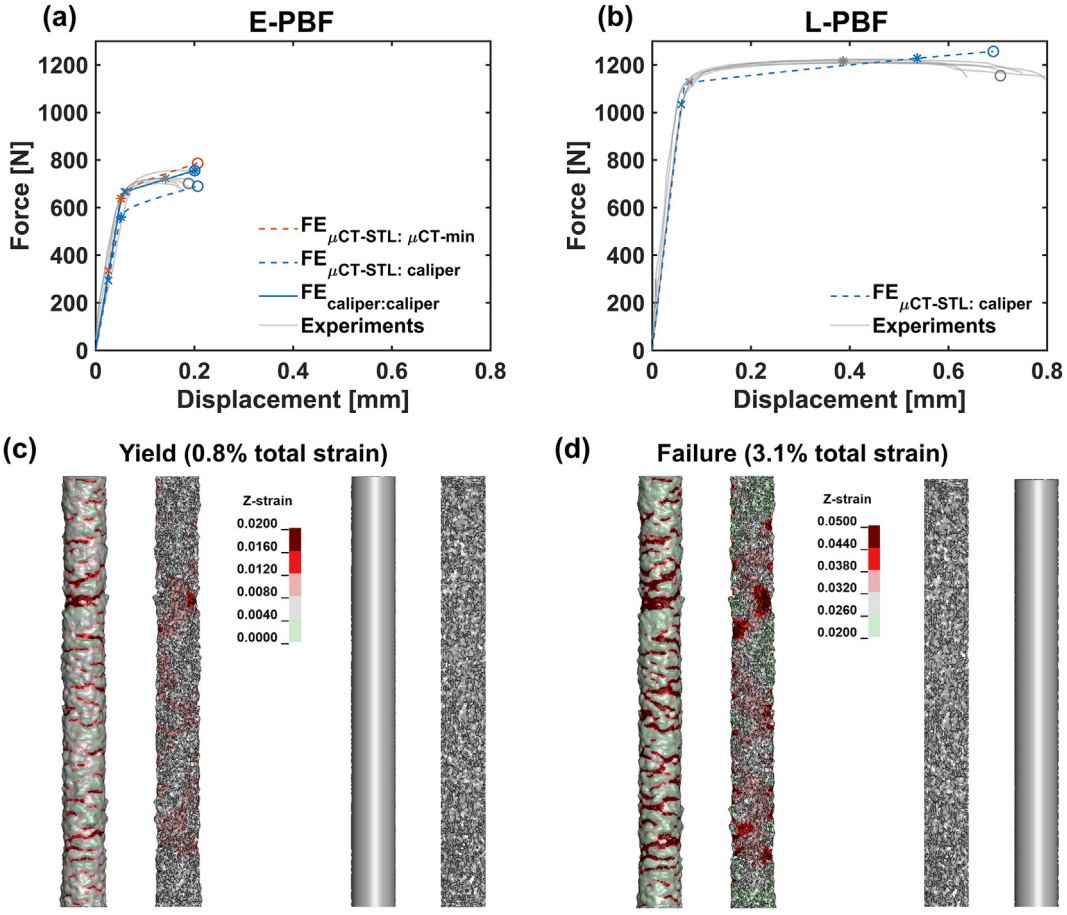

Fig. 6. The force–displacement response for experimental (grey) and simulated (blue and orange) tensile tests for as-printed E-PBF (a) and HIPed L-PBF (b) specimens. Simulations with dashed lines indicate the geometries based on the μCT-STL file and the simulation with solid line a geometry based on caliper measurements. The simulations used material inputs based on caliper measurements (blue) or minimum cross-section of the μCT geometry (orange). The yield (*) and ultimate tensile strength (x) in the experiment and for the first element in the simulation is indicated. Moreover, the failure stain in the experiment and the first element to reach failure strains in the simulation is marked (o). Strain maps are presented for E-PBF models, $FE_{\mu CT\text{-}STL:\ \mu CT\text{-}min}$ and $FE_{caliper:\ caliper}$, at yield (c) and at failure (d).

Table 3
Results from the E-PBF and L-PBF implant tests (average ± standard deviation).

Sample type	Construct stiffness [N/mm]	CaP fracture [N]	Displacement at CaP fracture [mm]	Global Peak load [N]	Displacement at peak load [mm]	Energy absorbed at peak load [J]
E-PBF	146 ± 9	319 ± 33	3.1 ± 0.2	457 ± 9	11.2 ± 0.3	3.1 ± 0.1
L-PBF [19]	156 ± 10	368 ± 18	3.2 ± 0.1	846 ± 40	11.7 ± 0.5	6.0 ± 0.4

combination with the μCT geometry ($FE_{\mu CT\text{-}STL:\ caliper}$). The combination of μCT geometry (STL-file) with a material input based on the minimum cross-sectional area from the μCT ($FE_{\mu CT\text{-}STL:\ \mu CT\text{-}min}$), resulted in a force–displacement response in agreement with the experimental tensile test results. However, the error in yield force and force at failure strain were 49.8% and 11.7%, respectively, calculated when the first element reached yield or failure. Moreover, the corresponding errors in strain was 59% and 64%. An idealized simulation of a cylinder with caliper-based dimensions and caliper-based material inputs ($FE_{caliper:\ caliper}$) resulted in a force-displacement response close to the corresponding experimental results. The error in yield force and force at failure strain were 0.08% and 4.5%, respectively, calculated when the first element reached yield or failure. The corresponding strains were also predicted with a lower error, 6% and 42%. In the E-PBF specimen, the effect of the rough surface in terms of stress concentration is demonstrated in Fig. 6a. For models with μCT-based geometry, elements that exceeded yield and failure strains were found much earlier than what would have been expected based on the experimental force–displacement response. These stress concentrations are clearly visible in the strain plots in Fig. 6c–d. For the simulations with a smooth cylinder, elements reaching yield and failure strains were in good agreement with yield and failure in the force–displacement response. For the models replicating the tensile tests with L-PBF specimen (Fig. 6b), a good agreement was observed for the model with μCT geometry of the L-PBF specimen and caliper-based material inputs ($FE_{\mu CT\text{-}STL:\ caliper}$). A difference of 8.4% and 1.0% was found for the yield and failure force respectively, calculated when the first element to reach yield or failure. Moreover, the corresponding errors in strain was 22% and 39%.

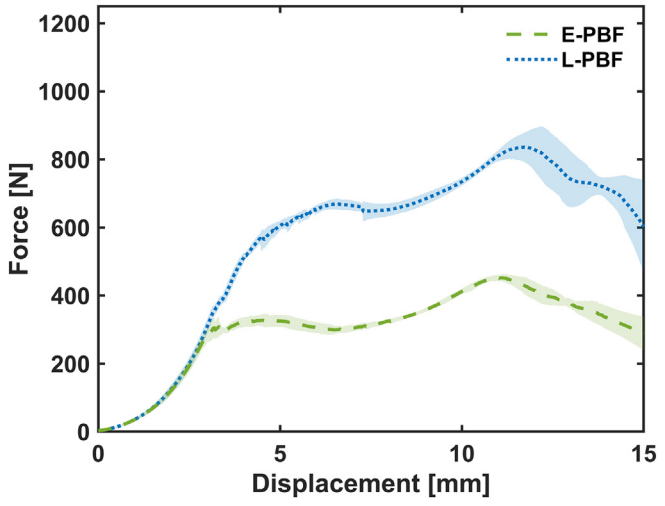

Fig. 7. Force vs. displacement response from the quasi-static implant testing. The average response for the as-printed E-PBF specimens (green dashed lines) and the HIPed L-PBF specimens (blue dotted lines) – from our previous study [19]. The standard deviations are plotted as a shaded area.

3.4. Mechanical testing of implant specimens

Results from the quasi-static test on the implants are summarized in Table 3 and Fig. 7. The data was analyzed before the force had dropped below 50% of the peak load. There was no significant difference in construct stiffness between the E-PBF and the L-PBF implant groups. The first CaP fracture was observed at a significantly lower load ($p = 0.013$) for the E-PBF (317 ± 34 N) compared to the L-PBF implants (368 ± 18 N). The displacement at which the first CaP fracture occurred was not significantly different between E-PBF and L-PBF. After CaP fracture, the load was lower throughout the test for the E-PBF specimens. The force started plateauing following the first CaP fracture in the E-PBF implants, whereas the force increased further in the L-PBF implants. Both the global peak load (457 ± 9 N vs. 846 ± 40 N) and displacement at peak load (11.2 ± 0.3 mm vs. 11.7 ± 0.5 mm) were significantly lower for the E-PBF specimens ($p < 0.05$). The energy absorbed throughout the test was also significantly lower ($p < 0.01$) for the E-PBF specimens.

3.5. Implant simulations

The experimental and simulated force–displacement response for the implant F*E*-models are provided in Fig. 8. Table 4 summarizes the results for the initial peak load (before 4 mm displacement) for the experiments and the F*E*-models. The L-PBF implant model with CAD based geometry and caliper based material input ($FE_{CAD:\ caliper}$) resulted in an 11% error in initial peak load compared to the experimental implant response. For the E-PBF, a large error (90%) was found in initial peak force when the CAD geometry was simulated with caliper based material input ($FE_{CAD:\ caliper}$). The error decreased to 33% when the reduced geometry was simulated with material properties based on the minimum μCT measurements ($FE_{\mu CT\text{-}min:\ \mu CT\text{-}min}$).

Overall, the reduction in geometry ($FE_{CAD:\ caliper}$ vs. $FE_{\mu CT\text{-}min:\ caliper}$) resulted in 39% reduction in initial peak load for implant simulations with L-PBF material inputs and in 34% reduction in initial peak load for implant simulations with E-PBF material inputs. Reduction in material inputs, from L-PBF to E-PBF, resulted in decreases of initial peak load of 16% for the simulations with the CAD geometry (L-PBF $FE_{CAD:\ caliper}$ vs. E-PBF $FE_{CAD:\ caliper}$) and 11% for the simulations with the reduced geometry (L-PBF $FE_{\mu CT\text{-}min:\ caliper}$ vs. E-PBF $FE_{\mu CT\text{-}min:\ caliper}$).

Table 4
Initial peak load for the experiments and the different implant FE-models.

	Material input L-PBF/E-PBF	Initial peak load [N]	Difference to experimental reference
Experiment L-PBF [19]	–	669	–
Experiment E-PBF	–	328	–
$FE_{CAD:\ caliper}$	L-PBF	743	+11.1%
$FE_{\mu CT\text{-}min:\ caliper}$	L-PBF	454	−32.1%
$FE_{CAD:\ caliper}$	E-PBF	624	+90.2%
$FE_{CAD:\ \mu CT\text{-}min}$	E-PBF	676	+106.1%
$FE_{\mu CT\text{-}min:\ caliper}$	E-PBF	409	+24.7%
$FE_{\mu CT\text{-}min:\ \mu CT\text{-}min}$	*E*-PBF	435	+32.6%

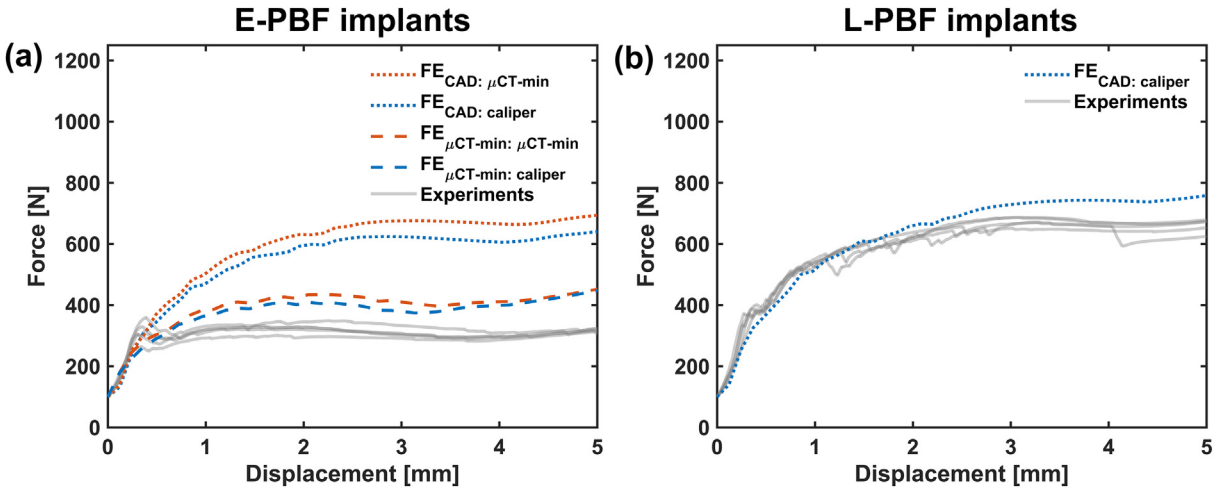

Fig. 8. Force vs. displacement response from the quasi-static implant testing and simulations: E-PBF (left) and L-PBF (right). The experimental responses are shown in grey. Simulations with dotted lines indicate a CAD-based geometry; dashed lines indicate a geometry based on the minimum CT cross-section. E-PBF implant simulations used material inputs based on caliper measurements (blue) or minimum cross-section of the μCT geometry (orange). L-PBF implant simulations used caliper-based material inputs (blue).

4. Discussion

The aim of this study was to compare the mechanical response of HIPed L-PBF and as-printed E-PBF Ti-6Al-4V tensile test specimens and CaP–Ti composite cranial implant specimens. In both the tensile and implant test, the mechanical behavior for the HIPed L-PBF specimens was superior to the as-printed E-PBF specimens as expected (46% lower peak force for the E-PBF specimen in the implant testing). Our second aim was to use FE-models to quantify the contribution that different material inputs and geometrical deviations had on the overall mechanical response of the CaP–Ti cranial implant specimens. Based on FE-models for the two manufacturing techniques, we found the geometrical differences between the tested implants to be the main factor in implant performance; with a 34–39% reduction in peak force base on geometry, and only a 11–16% reduction based on the material input.

Both the surface roughness and deviations in the designed versus the printed geometry were issues for the E-PBF specimens. In contrast, investigations on the HIPed L-PBF specimens found a smooth surface and no large deviations compared to the designed geometry. For both manufacturing methods, the surface roughness measurements (S_a and S_z) were in the range of previous studies [13,29]. Comparing the printed to the designed cross-sectional area, the E-PBF specimens had a negative average deviation of 18% in the tensile specimen, and 30% for specimens isolated from the implant structure. The low accuracy and rough surface for E-PBF in small dimensions have been observed previously [16,30–32]. Persenot et al. (2018) manufactured rods (ø = 2 mm) by E-PBF, and reported a 13% deviation between printed and designed cross-sectional area. Horn et al. (2016) manufactured lattice structures and measured the individual struts with diameters varying from 0.45 to 2.1 μm. For struts with a designed diameter of 0.45 and 0.58 mm a positive deviation was observed, while for diameters 0.72 to 2.1 mm a negative deviation was observed (maximum −37% in cross-sectional area). In contrast, another study reported no significant deviations on rods with a designed diameter of 0.8 mm as compared to the manufactured rods (ø = 0.77 ± 0.4 mm) [33]. Some of these studies have reported that less geometrical deviation and a lower surface roughness is achieved for specimen printed vertically along the build direction, compared to specimens printed with an oblique angle towards the build direction [16,31,32]. This was also noticed in our study, where the tensile specimens were built vertically and the implant specimens with an angle. All the mentioned studies used machines from Arcam (Arcam AB, Sweden), similar to our study.

A comparison of ultimate tensile stresses from this study and previous studies are presented in Fig. 9. The ultimate tensile stresses from this study were calculated with the cross-sectional areas based on the caliper measurements, 738 ± 26 MPa and 1086 ± 10 MPa for E-PBF and L-PBF, respectively. According to ASTM F136 '*the Standard Specification for Wrought Ti6Al4V for Surgical Implant Applications*' [34], the σ_{UTS} should be above 860 MPa, which was reached for the HIPed L-PBF specimens, but not for the as-printed E-PBF specimens. However, when the tensile force was calculated by the minimum cross-sectional area from the μCT, a σ_{UTS} of 842 MPa was obtained for E-PBF (14% increase compared to the caliper based σ_{UTS}). Other studies on as-printed E-PBF specimens with small geometries have found similar values (Fig. 9) [13,16]. One study (on rod specimens, ø = 2 mm) reported a σ_{UTS} of 721 MPa, which increased to 870 MPa if the minimum cross-sectional area from μCT measurements was used [16]. Algardh et al. (2016) investigated rectangular specimens with a wall-thickness varying between 0.5 mm to 5 mm, as well as different layer thicknesses and powders with different average particle sizes [13]. Lower σ_{UTS} was observed for a smaller wall-thickness, where a σ_{UTS} around 700 MPa was reported for specimens with 1 mm wall-thickness. An improvement was reported if a smaller powder size and layer thickness was used, which resulted in lower surface roughness. A part of the explanation for this improvement in σ_{UTS} could be that a lower surface roughness would give a better estimation of the cross-sectional area, since it was based on measurements by calipers. For standard sized specimens, both as-printed and machined, a higher σ_{UTS} has been observed [35,36]. In these studies, L-PBF and E-PBF printed material have shown similar tensile strength when heat treatment was applied to the L-PBF specimen [35,36]. The L-PBF specimens from our study had similar σ_{UTS} as the standard sized specimens (Fig. 9).

The hardness measurements confirmed the large influence of the high surface roughness in the tensile tests for the as-printed E-PBF specimen. The relation between hardness and yield strength is typically linear. In our study, the microhardness was 10% lower for the as-printed E-PBF as compared to the HIPed L-PBF specimen, whereas the yield strength was 48% lower.

The deviations in geometry and the high surface roughness made numerical modelling of the E-PBF specimens challenging. For the tensile specimen, an agreement between experimental and modelled force–displacement response was observed if the actual geometry (STL-file from the μCT) was used together with the material inputs derived with the minimum or caliper cross-sectional area. However, the calculation of a failure strain remains difficult. FE-models of the tensile

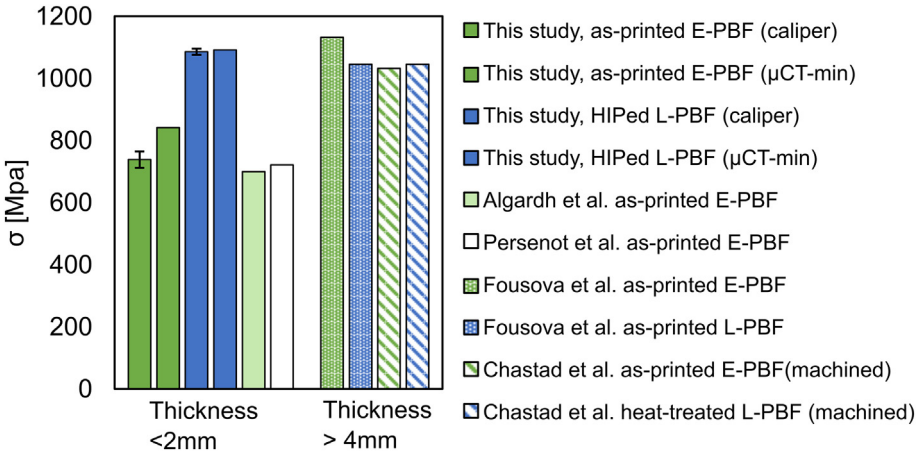

Fig. 9. Comparison of results obtained in this study (using the caliper measurements) and previous studies from the literature in terms of σ_{UTS} for E-PBF (green) and L-PBF (blue) specimens. The light green and white bars are from studies using as-printed specimens of similar size as in the present study (thickness <2 mm), and where the cross-sectional area was obtained using caliper measurements (Algardh et al.) or CAD-geometry (Persenot et al.). The patterned bars are from studies using standard sized specimens (both machined and as-printed).

specimens indicated much higher local strains due to the surface roughness of the specimens. This indicates that for smooth specimens the failure strain could be much higher. In the simulated vs. experimental force–displacement response for the implants, a more accurate outcome was obtained when the cross-section of the titanium structure was reduced to the minimum measurements obtained by μCT, instead of using the CAD-geometry. However, the force was still overpredicted by 33% with this geometry. As our previous study validated a *FE*-model of the L-PBF produced implants with higher accuracy (11% difference to the experimental result in initial peak force) [20], the results for the E-PBF implant FE-models in this study implies that either the geometry of the titanium structure is still not well represented, or that ceramic failure due to the thinner structures is even more challenging to capture with the limitations of the material inputs. As previously mentioned, it is known that the geometrical deviations for the E-PBF can vary depending on the angle at printing [16]. There was less deviation in the E-PBF tensile specimen (printed vertically) than in the implant rods (printed with an oblique angle from the printing direction). In order to accurately model the implant specimen, the deviations in the geometry must be further evaluated across the whole implant structure. Similar conclusions regarding numerical modelling and geometrical deviations by E-PBF were reached in a previous study [31]. The effect of deviations in geometrical accuracy and surface defects, in designed vs. printed structures has been more commonly investigated for L-PBF structures, although for even smaller dimensions [37,38]. In a lattice structure with a strut thickness ~ 0.3 mm, Liu et al. (2017) found a 47% difference in compressive strength when comparing the experimental results to the *FE*-predictions based on the designed geometry. By taking strut waviness, strut thickness variation, and strut oversizing from μCT analysis into account, the prediction compared to the experiments improved to a 13% difference [38]. In our study we only considered the geometrical deviations in terms of diameter of the rods in the mesh implant structure.

The deviations in geometry for the E-PBF process are due to the high working temperature, shrinkage of the material and un-melted powder that attaches to the printed part [32,39]. The size limitation in manufacturing thin structures by E-PBF is related to the size of the minimum volume of melted material, which is in the range of the electron beam spot size. The beam spot size for the E-PBF (200–1000 μm) is considerably larger compared to that of the L-PBF process (30–250 μm) [40]. Improvements of the *E*-PBF process could reduce the surface roughness and decrease the geometrical deviations. There are several E-PBF process parameters which affect both microstructure and surface roughness, such as preheating, beam current, scanning speed, layer thickness, powder particle size, re-use of powder, number and design of the contours [13,41–45]. Several interesting experimental methods have been evaluated for E-PBF printed Ti-6Al-4V [16,46–48]. For improving the surface roughness, post-processing by chemical etching or electro-polishing seems particularly promising [16,46]. The aforementioned potential process improvements could be important for the use of E-PBF in the CaP–Ti implants, and should be investigated in future studies. However, a rough surface topology on E-PBF printed samples has been found to be biologically beneficial for blood coagulation in vitro [14] and osseointegration in vivo [15].

A limitation of our study was that we did not investigate the microstructure nor defects on a micro-level e.g. micro-porosity. However, this has been investigated and compared between E-PBF and L-PBF for Ti-6Al-4V in previous studies [29,35,36,49]. L-PBF as-printed Ti-6Al-4V structures have an initial α´-martensitic microstructure due to the large differences in temperature during the process. As HIP takes place at an increased temperature followed by cooling under controlled conditions, the martensitic phase transforms into a lamellar structure with a mixture of α and β phases [49]. Similar microstructures can also be reached by heat treatment at the same temperatures as the HIP [49]. For as-printed vs. HIPed L-PBF parts, the change in microstructure affects the mechanical properties. The ultimate tensile stress and yield strength decreases, but the ductility is improved after HIP [49]. The E-PBF process takes place at a high temperature (>700 °C) which results in a microstructure with α and β phases for as-printed parts [16,36]. The mechanical properties are affected also for E-PBF printed parts after HIP (due to a coarsening of the α-lamellas) but to a lesser extent than for L-PBF printed material. In this study, the E-PBF parts and the HIPed L-PBF parts likely have a similar microstructure, with α and β phases. Microstructural observations would not change the material input for the *FE*-models. Consequently, the conclusion of our study – that the difference in the implant response is explained by the geometrical deviations in the titanium structures – would not be affected.

For future studies, it would be interesting to include more groups in the tensile tests. For example, a group with E-PBF specimens in the CAD dimensions with a smooth, e.g. machined, surface. It would also be interesting to include specimens with several printing directions in order to further characterize how the printing directions of the implants affect the dimensional accuracy. Furthermore, in future studies each individual specimen should be characterized with μCT prior to testing to be able to investigate which type of defects initiate fracture. This would also improve the description of the geometry and the material inputs for the numerical models. With the current process parameters in

the application of the CaP–Ti implants, the use of E-PBF requires a redesign by upscaling the dimensions, and/or further post-processing of the printed surfaces, if a strength similar to L-PBF should be reached. If the issues regarding these factors are resolved for E-PBF, the time efficient production makes it a promising technology for on-demand production of patient-specific implants.

5. Conclusions

In conclusion, the dimensional accuracy for the E-PBF method is insufficient to obtain a mechanical strength similar to the L-PBF printed CaP–Ti implants. The mechanical strength of the as-printed E-PBF compared to the HIPed L-PBF specimens was significantly lower in both the material tensile tests (47%) and full implant tests (85%). The computational analysis indicated that the geometrical differences was the main contributor to the inferior mechanical response of the as-printed E-PBF implants: a 34–39% reduction in initial peak force was observed due to geometry, and only a 11–16% reduction due to material input. The use of E-PBF in this application requires a redesign by upscaling the dimensions and/or further post-processing of the as-printed surfaces, in order to reach a strength similar to the HIPed L-PBF. This study supports the importance of evaluating the manufacturing technique in the dimensions and printing directions of the final application.

Data availability statement

Data will be made available on request.

Credit author statement

Susanne Lewin: Conceptualization, Investigation, Visualization, Methodology, Writing - original draft, Writing - review & editing. *Ingmar Fleps:* Conceptualization, Investigation, Visualization, Methodology, Writing - review & editing. *Jonas Åberg:* Conceptualization, Methodology, Writing - review & editing. *Håkan Engqvist:* Conceptualization, Funding acquisition, Writing - review & editing. *Stephen J. Ferguson:* Conceptualization, Funding acquisition, Writing - review & editing. *Caroline Öhman-Mägi:* Supervision, Writing - review & editing. *Benedikt Helgason:* Conceptualization, Methodology, Supervision, Writing - review & editing. *Cecilia Persson:* Conceptualization, Methodology, Supervision, Writing - review & editing, Funding acquisition.

Declaration of Competing Interest

The authors declare the following financial interests/personal relationships which may be considered as potential competing interests: Dr. Åberg and Prof. Engqvist have consulting agreements with OssDsign and also direct ownership in OssDsign. Prof. Engqvist is on the board of OssDsign.

Acknowledgements

Funding from the Eurostars-2 Joint European Union's Horizon 2020 (E19741) and support from Sweden's Innovation Agency VINNOVA (AddLife Competence Centre, 2019-00029) are gratefully acknowledged.

References

[1] M. Lowther, et al., Clinical, industrial, and research perspectives on powder bed fusion additively manufactured metal implants, Additive Manufacturing 28 (2019) 565–584, https://doi.org/10.1016/j.addma.2019.05.033.

[2] T. Zegers, M. ter Laak-Poort, D. Koper, B. Lethaus, P. Kessler, The therapeutic effect of patient-specific implants in cranioplasty, J. Cranio-Maxillofac. Surg. 45 (1) (2017) 82–86, https://doi.org/10.1016/j.jcms.2016.10.016.

[3] L. Kihlström Burenstam Linder, U. Birgersson, K. Lundgren, C. Illies, T. Engstrand, Patient-specific titanium-reinforced calcium phosphate implant for the repair and healing of complex cranial defects, World Neurosurgery (2018), https://doi.org/10.1016/j.wneu.2018.10.061.

[4] B. Lethaus, M. Bloebaum, D. Koper, M. Poort-ter Laak, P. Kessler, Interval cranioplasty with patient-specific implants and autogenous bone grafts – success and cost analysis, J. Cranio-Maxillofac. Surg. 42 (8) (2014) 1948–1951, https://doi.org/10.1016/j.jcms.2014.08.006.

[5] I.P. Janecka, New reconstructive Technologies in Skull Base Surgery: role of titanium mesh and porous polyethylene, Arch. Otolaryngol. Head Neck Surg. 126 (3) (2000) 396–401, https://doi.org/10.1001/archotol.126.3.396.

[6] T. DebRoy, et al., Scientific, technological and economic issues in metal printing and their solutions, Nat. Mater. 18 (10) (2019) 1026–1032, https://doi.org/10.1038/s41563-019-0408-2.

[7] B.P. Conner, et al., Making sense of 3-D printing: creating a map of additive manufacturing products and services, Additive Manufacturing 1 (2014) 64–76, https://doi.org/10.1038/s41563-019-0408-2.

[8] S.L. Sing, J. An, W.Y. Yeong, F.E. Wiria, Laser and electron-beam powder-bed additive manufacturing of metallic implants: a review on processes, materials and designs, J. Orthop. Res. 34 (3) (2016) 369–385, https://doi.org/10.1002/jor.23075.

[9] Y. Kok, et al., Anisotropy and heterogeneity of microstructure and mechanical properties in metal additive manufacturing: a critical review, Mater. Des. 139 (2018) 565–586, https://doi.org/10.1016/j.matdes.2017.11.021.

[10] X.Z. Zhang, M. Leary, H.P. Tang, T. Song, M. Qian, Selective electron beam manufactured Ti-6Al-4V lattice structures for orthopedic implant applications: current status and outstanding challenges, Curr. Opinion Solid State Mater. Sci. 22 (3) (2018) 75–99, https://doi.org/10.1016/j.cossms.2018.05.002.

[11] S. Liu, Y.C. Shin, Additive manufacturing of Ti6Al4V alloy: a review, Mater. Des. 164 (2019) 107552, https://doi.org/10.1016/j.matdes.2018.107552.

[12] V. Weißmann, P. Drescher, R. Bader, H. Seitz, H. Hansmann, N. Laufer, Comparison of single Ti6Al4V struts made using selective laser melting and electron beam melting subject to part orientation, Metals vol. 7 (3) (2017) 91, https://doi.org/10.3390/met7030091.

[13] J. K. Algardh et al., Thickness dependency of mechanical properties for thin-walled titanium parts manufactured by Electron Beam Melting (EBM)®, Additive Manufacturing, vol. 12, pp. 45–50, 10-01 2016, doi: 10.1016/j.addma.2016.06.009.

[14] R.K. Ek, J. Hong, A. Thor, M. Bäckström, L.-E. Rännar, Micro-to macroroughness of additively manufactured titanium implants in terms of coagulation and contact activation, Int. J. Oral Maxillofac. Implants vol. 32 (3) (2017), https://doi.org/10.11607/jomi.5357.

[15] D.S. Ruppert, O.L.A. Harrysson, D.J. Marcellin-Little, L.E. Dahners, P.S. Weinhold, Improved osseointegration with as-built electron beam melted textured implants and improved peri-implant bone volume with whole body vibration, Med. Eng. Phys. 58 (2018) 64–71, https://doi.org/10.1016/j.medengphy.2018.05.003.

[16] T. Persenot, G. Martin, R. Dendievel, J.-Y. Buffiére, E. Maire, Enhancing the tensile properties of EBM as-built thin parts: Effect of HIP and chemical etching, Mater. Charact. 143 (2018) 82–93, https://doi.org/10.1016/j.matchar.2018.01.035.

[17] T. Engstrand, et al., Development of a bioactive implant for repair and potential healing of cranial defects, J. Neurosurg. 120 (1) (2014) 273–277, https://doi.org/10.3171/2013.6.JNS1360.

[18] T. Engstrand, L. Kihlström, K. Lundgren, M. Trobos, H. Engqvist, P. Thomsen, Bioceramic implant induces bone healing of cranial defects, Plast Reconstr Surg Glob Open vol. 3 (8) (2015), https://doi.org/10.1097/GOX.0000000000000467.

[19] S. Lewin, et al., Mechanical behaviour of composite calcium phosphate–titanium cranial implants: Effects of loading rate and design, J. Mech. Behav. Biomed. Mater. vol. 104 (2020) 103701, https://doi.org/10.1016/j.jmbbm.2020.103701.

[20] S. Lewin, et al., Implicit and explicit finite element models predict the mechanical response of calcium phosphate-titanium cranial implants, J. Mech. Behav. Biomed. Mater. (2020) 104085, https://doi.org/10.1016/j.jmbbm.2020.104085.

[21] B. Laure, F. Tranquart, L. Geais, D. Goga, Evaluation of skull strength following parietal bone graft harvest, Plast. Reconstr. Surg. 126 (5) (2010) 1492–1499.

[22] D. Garcia-Gonzalez, et al., On the mechanical behaviour of PEEK and HA cranial implants under impact loading, J. Mech. Behav. Biomed. Mater. 69 (2017) 342–354, https://doi.org/10.1016/j.jmbbm.2017.01.012.

[23] N. Otsu, A threshold selection method from gray-level histograms, IEEE Transactions on Systems, Man, and Cybernetics 9 (1) (1979) 62–66, https://doi.org/10.1109/TSMC.1979.4310076.

[25] J. Bonet, A.J. Burton, A simple average nodal pressure tetrahedral element for incompressible and nearly incompressible dynamic explicit applications, Commun. Numer. Methods Eng. 14 (5) (1998) 437–449, https://doi.org/10.1002/(SICI)1099-0887(199805)14:5<437::AID-CNM162>3.0.CO;2-W.

[26] I. Ajaxon, et al., Elastic properties and strain-to-crack-initiation of calcium phosphate bone cements: revelations of a high-resolution measurement technique, J. Mech. Behav. Biomed. Mater. 74 (2017) 428–437, https://doi.org/10.1016/j.jmbbm.2017.06.023.

[27] E. Charrière, et al., Mechanical characterization of brushite and hydroxyapatite cements, Biomaterials 22 (21) (2001) 2937–2945, https://doi.org/10.1016/S0142-9612(01)00041-2.

[28] R Core Team, R: A language and environment for statistical computing. R Foundation for Statistical Computing, Vienna, Austria. URL http://www.R-project.org/, 2014.

[29] M. Kahlin, H. Ansell, J.J. Moverare, Fatigue behaviour of notched additive manufactured Ti6Al4V with as-built surfaces, Int. J. Fatigue 101 (2017) 51–60, https://doi.org/10.1016/j.ijfatigue.2017.04.009.

[30] T.J. Horn, O. Harrysson, D.J. Marcellin-Little, H.A. West, B.D.X. Lascelles, R. Aman, Flexural properties of Ti6Al4V rhombic dodecahedron open cellular structures fabricated with electron beam melting, Additive Manufacturing 1–4 (2014) 2–11, https://doi.org/10.1016/j.addma.2014.05.001.

[31] M. Suard, et al., Mechanical equivalent diameter of single struts for the stiffness prediction of lattice structures produced by Electron beam melting, Additive Manufacturing 8 (2015) 124–131.
[32] M. Galati, P. Minetola, G. Rizza, Surface roughness characterisation and analysis of the Electron Beam Melting (EBM) process, Materials 13 (2019), https://doi.org/10.3390/ma12132211 Art. no. 13.
[33] W. Van Grunsven, E. Hernandez-Nava, G.C. Reilly, R. Goodall, 'Fabrication and Mechanical Characterisation of Titanium Lattices with Graded Porosity, Metals vol. 4 (3) (2014), https://doi.org/10.3390/met4030401 Art. no. 3.
[34] F04 Committee, 'ASTM F136: Specification for Wrought Titanium-6Aluminum-4Vanadium ELI (Extra Low Interstitial) Alloy for Surgical Implant Applications (UNS R56401)', ASTM International. https://doi.org/10.1520/F0136-13.
[35] V. Chastand, P. Quaegebeur, W. Maia, E. Charkaluk, Comparative study of fatigue properties of Ti-6Al-4V specimens built by electron beam melting (EBM) and selective laser melting (SLM), Mater. Charact. 143 (2018) 76–81, https://doi.org/10.1016/j.matchar.2018.03.028.
[36] M. Fousová, D. Vojtěch, K. Doubrava, M. Daniel, C.-F. Lin, Influence of Inherent Surface and Internal Defects on Mechanical Properties of Additively Manufactured Ti6Al4V Alloy: Comparison between Selective Laser Melting and Electron Beam Melting, Materials vol. 11 (4) (2018) 537, https://doi.org/10.3390/ma11040537.
[37] D. Melancon, Z.S. Bagheri, R.B. Johnston, L. Liu, M. Tanzer, D. Pasini, Mechanical characterization of structurally porous biomaterials built via additive manufacturing: experiments, predictive models, and design maps for load-bearing bone replacement implants, Acta Biomater. 63 (2017) 350–368, https://doi.org/10.1016/j.actbio.2017.09.013.
[38] L. Liu, P. Kamm, F. García-Moreno, J. Banhart, D. Pasini, Elastic and failure response of imperfect three-dimensional metallic lattices: the role of geometric defects induced by selective laser melting, J. Mech. Phys. Solids 107 (2017) 160–184, https://doi.org/10.1016/j.jmps.2017.07.003.
[39] G. Del Guercio, M. Galati, A. Saboori, P. Fino, L. Iuliano, Microstructure and mechanical performance of Ti–6Al–4V lattice structures manufactured via Electron beam melting (EBM): a review, Acta Metall. Sin. (Engl. Lett.) 33 (2) (2020) 183–203, https://doi.org/10.1007/s40195-020-00998-1.
[40] B. Wysocki, P. Maj, R. Sitek, J. Buhagiar, K.J. Kurzydłowski, W. Święszkowski, Laser and electron beam additive manufacturing methods of fabricating titanium bone implants, Appl. Sci. vol. 7 (7) (2017), https://doi.org/10.3390/app7070657.
[41] P. Wang, W. J. Sin, M. L. S. Nai, and J. Wei, 'Effects of processing parameters on surface roughness of additive manufactured Ti-6Al-4V via electron beam melting', *Materials*, vol. 10, no. 10, p. 1121, 2017.
[42] R.K. Ek, L.-E. Rännar, M. Bäckstöm, P. Carlsson, The effect of EBM process parameters upon surface roughness, Rapid Prototyp. J. 22 (3) (2016) 495–503, https://doi.org/10.1108/RPJ-10-2013-0102.
[43] R. Tosi, E. Muzangaza, S. Nonni, P.J. Withers, P.D. Lee, Effect of preheating on the thermal, microstructural and mechanical properties of selective electron beam melted Ti-6Al-4V components, Mater. Des. 174 (2019) 107792, https://doi.org/10.1016/j.matdes.2019.107792.
[44] R. Schur, et al., A Fractographic analysis of additively manufactured Ti6Al4V by Electron beam melting: effects of powder reuse, J. Fail. Anal. Prev. 20 (3) (2020) 794–803, https://doi.org/10.1007/s11668-020-00875-0.
[45] S. Ghods, et al., Electron beam additive manufacturing of Ti6Al4V: evolution of powder morphology and part microstructure with powder reuse, Materialia 9 (2020) 100631, https://doi.org/10.1016/j.mtla.2020.100631.
[46] V. Urlea, V. Brailovski, Electropolishing and electropolishing-related allowances for powder bed selectively laser-melted Ti-6Al-4V alloy components, J. Mater. Process. Technol. 242 (2017) 1–11, https://doi.org/10.1016/j.jmatprotec.2016.11.014.
[47] E. Chudinova, et al., Surface modification of Ti6Al4V alloy scaffolds manufactured by electron beam melting, J. Phys. Conf. Ser. vol. 1145 (2019) 012030, https://doi.org/10.1088/1742-6596/1145/1/012030.
[48] D. Khrapov, et al., The impact of post manufacturing treatment of functionally graded Ti6Al4V scaffolds on their surface morphology and mechanical strength, J. Mat. Res. Technol. 9 (2) (2020) 1866–1881, https://doi.org/10.1016/j.jmrt.2019.12.019.
[49] X. Yan, et al., Effect of heat treatment on the phase transformation and mechanical properties of Ti6Al4V fabricated by selective laser melting, J. Alloys Compd. 764 (2018) 1056–1071, https://doi.org/10.1016/j.jallcom.2018.06.076.